Current **A**pplied **S**cience and **T**echnology e-ISSN: 2586-9396

Curr. Appl. Sci. Technol. ….., Vol... (No...), e0266426

Research article

Preparation of Composite Films of Rod-like Structure of ZnO and Corn Starch for Bending Sensor

Kitikamol Feemuchang, Korakot Onlaor, Benchapol Tunhoo* and Thutiyaporn Thiwawong

Electronics and Control Systems for Nanodevices Research Laboratory, Department of Nanoscience and Nanotechnology, School of Integrated Innovative Technology, King Mongkut's Institute of Technology Ladkrabang, Bangkok 10520, Thailand

Received: 24 February 2025, Revised: 26 May 2025, Accepted: 8 June 2025, Published: 10 October 2025

Abstract

In this work, rod-like structure zinc oxide (R-ZnO) was synthesized by a hydrothermal process with the hydrothermal times of 3, 5, and 10 h. The effect of reaction time was reflected in the physical properties of the prepared R-ZnO, such as crystalline structure, shape geometries, and optical properties. Then, a bending device was fabricated with starch composite films and the rod-like structure of zinc oxide with different R-ZnO concentrations. The fabricated device exhibited flexibility characteristics at various bending angles. The composite film of corn starch and 1%wt. R-ZnO at a hydrothermal reaction time of 10 h demonstrated a high sensitivity at 89.5% with a gauge factor of 1.58. Moreover, the device of corn starch composited with R-ZnO exhibited fast response/recovery time of 0.23/0.15 s with high stability of bending cycle of more than 1,600 cycles. Therefore, the composite films of R-ZnO and natural starch are strong potential candidates for bending devices.

Keywords: bending sensor; ZnO; starch composite films

1. Introduction

Wearable and flexible electronics, including innovative textile technology, have played remarkable roles in many applications, ranging from smart healthcare devices to interactive robotics. Among these, bending sensors have become an important key for those applications because they can detect the physical parameters, such as bending radius, strain values, etc. (Costa et al., 2019; Muhammad & Kim, 2023). Typically, a conventional bending sensor is often fabricated on synthetic polymers or metals; nevertheless, the use of these materials poses challenges related to environmental sustainability and flexibility (Azmi et al., 2022). Natural biopolymers have emerged as promising alternative materials in recent years due to their advantages and properties, such as cost-effectiveness, biocompatibility, and biodegradability. Corn starch is a naturally derived polymer that has been paid much attention to for its potential as a bending matrix in sensor applications.

*Corresponding author: E-mail: benchapol.tu@kmitl.ac.th
https://doi.org/10.55003/cast.2025.266426

Corn starch is a naturally abundant and biodegradable polymer that has been widely investigated as a base material for eco-friendly films due to its film-forming properties. However, it faces limitations in mechanical strength and water resistance (Sun et al., 2019). Those drawbacks can be compensated by adding additives such as modifiers or plasticizers, which are crucial in enhancing the flexibility and durability of the starch matrix as they reduce intermolecular forces, making the composite more suitable for practical applications (Vieira et al., 2011; Arifin et al., 2022). In addition, the development of bending sensors has seen notable progress in integrating biocompatible polymers and metal oxide nanomaterials, particularly in applications for wearable electronics and environmental monitoring.

Flexible sensors based on composite materials have received considerable attention (Guzenko et al., 2023). Those devices are based on a sensing layer with composite material between polymer matrix and filler materials. The polymer matrix is the primary host material used to prepare the sensing film layer. The filler materials include metal oxide nanoparticles, silver nanoparticles, and carbon materials such as carbon nanotubes, graphene, carbon black, etc. (Amjadi et al., 2014; Spinelli et al., 2018; Ferreira et al., 2019; Guzenko et al., 2023), which were used to employ conductive composite materials in piezoresistive sensors. These composite materials demonstrate high electrical sensitivity and good mechanical properties.

Zinc oxide (ZnO) has garnered considerable attention as an ideal material for bending sensing applications due to its unique structural, electrical, and optical properties. ZnO, which has a hexagonal wurtzite structure, provides a wide band gap of 3.37 eV and a high exciton binding energy, enabling stable performance even at room temperature (Song & Lim, 2007; Rathod et al., 2018; Shitu et al., 2024). Further, incorporating ZnO nanoparticles into plasticized starch matrix produced significant improvements in tensile strength, water resistance, and functional properties such as antibacterial activity and responsiveness in sensor applications (Ejsmont & Goscianska, 2023; Joongpun et al., 2024). Additionally, rod-like structure zinc oxide (R-ZnO) can be synthesized through cost-effective and environmentally friendly hydrothermal methods, allowing precise control over morphology and particle size under relatively low-temperature conditions (Kale et al., 2014). This method makes R-ZnO highly suitable for applications requiring sensitivity and stability, such as bending or curvature sensors (Yahiya et al., 2020). Rod-like structure ZnO, known for its excellent piezoelectric and semiconducting properties, can significantly enhance the sensing performance, enabling precise detection of mechanical deformation (Yang et al., 2017; Wasly et al., 2018).

This work presents a novel approach to fabricating and characterizing a bending sensor device. This device is based on a composite material composed of R-ZnO, synthesized through a hydrothermal process with various reaction time conditions, and corn starch film, which was modified to enhance bending sensitivity with the R-ZnO. With the rod-like structure of R-ZnO, the sensing behavior of the prepared device can be improved. The electrical responses of the device were analyzed under bending and external compressive forces, aiming to investigate the electrical behavior of zinc oxide within the corn starch matrix and its impact on the changes in device resistance.

2. Materials and Methods

2.1 Synthesis process for rod-like structure of ZnO

The precursor materials of ZnO preparation were zinc acetate dihydrate ($Zn(CH_3COO)_2.2H_2O$; 99-102%, SIGALD), sodium hydroxide (NaOH; ≥99%, analysis grade, EMSURE), glycerol ($C_3H_8O_3$; ≥99.5%, KemAus), gum arabic powder (99.5%, food grade, Chemipan, Thailand), corn starch (organic corn 100%, food grade, Mcgarrett, Thailand), respectively. The hydrothermal technique was employed to synthesize R-ZnO. First, 4.39 g of zinc acetate dihydrate were dissolved separately in 50 mL of deionized water, and 8 g of sodium hydroxide were dissolved in another 50 mL. Both precursor solutions were stirred to get a well-dissolved solution. Then, the NaOH solution was gradually mixed with zinc acetate and stirred on a laboratory hotplate at 80°C. The mixture was stirred for 1 h to initiate the preliminary growth of ZnO. After that, the mixture solution was transferred to a 120 mL Teflon-lined autoclave and heated in an oven to a temperature of 120°C for 3, 5, and 10 h, respectively. Those hydrothermal times were suitable for preparing the rod-like structure of ZnO. Generally, the properties of synthesized materials depend on the hydrothermal process growth time. In the case of ZnO rod-like structures, the longer the growth time was conducted, the longer the rods were, and the rod diameter increased. With excess growth time, nucleation process might reduce the rod-like structure and the crystallinity of prepared ZnO material (Khai et al., 2022). After completely cooling to room temperature, the synthesized material was washed and rinsed with deionized water to achieve a neutral pH and dried in a hot air convection oven at 60°C for 24 h.

The physical properties of the R-ZnO, including crystalline structure, morphology, chemical bonding vibrations, and functional groups were characterized using X-ray diffractometry technique (XRD, Rigaku SmartLab), scanning electron microscope (SEM, Hitachi SU-8230), Raman spectroscopy (Thermo Scientific™ DXR3 SmartRaman), and Fourier transform infrared spectroscopy (FTIR, PerkinElmer Spectrum Two). The optical bandgap energy of the material was measured using a UV-VIS-NIR spectrophotometer (HITACHI, UH4150).

2.2 Preparation of starch composite film

The procedure to prepare the starch-composite (SC) film for the sensing layer of the bending device was adapted from the method of Muhammad and Kim (2023). A 3.5% (w/v concentration) corn starch solution was prepared by dissolving the corn starch in the 85 mL of distilled water, while a 1% (wt/v) R-ZnO in distilled water was separately dispersed. R-ZnO acts as the filler to the starch matrix. It exhibits a high aspect ratio of rod-like structure that can distribute applied stress more evenly upon bending. The electrical properties of the composite film with R-ZnO change in inter-rod spacing and contact area when the composite film is bent. These microstructural perturbations transfer into significant resistance variations (Ma et al., 2016). The corn starch solution was stirred at 2000 rpm and heated using a magnetic stirrer. When the temperature reached 40°C, 1% (w/v) of gum arabic was added. The gum arabic acts as both an emulsifier and an aqueous starch solution, improving production film with uniformity. This ensured that the conductive pathways formed by the R-ZnO network remained continuous and reproducible under bending stress (Apandi et al., 2013). At a temperature of 62°C, where starch gelatinization occurs, 2% (v/v) of glycerol was added to the mixture. Glycerol was used as a plasticizer that intercalates the starch polymer chains and interchain hydrogen bonding. It enhances

product ductility and prevents brittleness. Glycerol can increase the flexibility of the plasticized film, which allows mechanical deformations to be fully transferred to the ZnO network to improve the sensitivity of the device (Żołek-Tryznowska & Cichy, 2018). At this gelation temperature, the onset starch suspension caused the granules to swell, rupture, and release amylose into the aqueous phase without molecule structure damage. Then, the suspension formed a viscous semi-gel. With this phase, the additives such as gum arabic, glycerol, and R-ZnO became uniformly dispersed with the absence of phase separation (Rittenauer et al., 2021).

Then, the final solution to be used to produce homogeneous composite films was prepared. The stirring continued until the temperature rose to 70°C, after which the mixture was cooled to 42°C. The viscosity characteristic of the final solution was measured by rheological measurement (Thermo Scientific, MARS 40 Rheometer). Finally, 7 mL of the final solution was poured into a plastic mold with dimensions of 3 x 5 cm and dried in a convection oven at 50°C and 20% relative humidity for 10 h. The prepared samples were categorized based on the synthesis of R-ZnO as pristine starch (without R-ZnO), SC R-ZnO 3, 5, and 10 h, respectively. The prepared pristine starch films and SC films are demonstrated in Figure 1. The figure inset of each figure shows the cross-section of films to achieve the thickness of prepared samples.

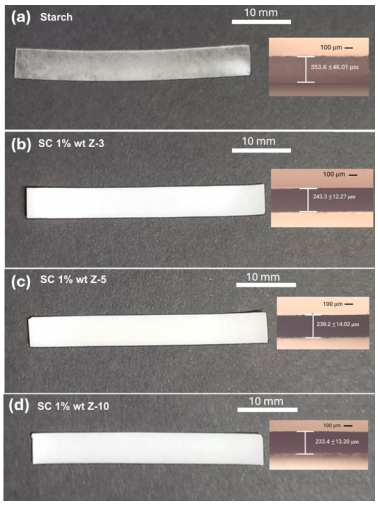

Figure 1. Photograph of (a) pristine starch film and SC R-ZnO films at various hydrothermal times of (b) Z-3, (c) Z-5, and (d) Z-10 for R-ZnO 3, 5, and 10 h, respectively. The inset images in each figure show the thickness of the prepared film.

2.3 Fabrication process of bending sensor

In preparing the bending sensor from the SC film, the film was cut to 4 x 0.5 cm dimensions. A mesh aluminum electrode (100 mesh per inch) with dimensions of 7 x 0.4 cm was used as the electrodes of the device, and the top and bottom electrodes were perpendicularly aligned. The electrodes were then arranged as shown in Figure 2a. The fabricated device is shown in Figure 2b. In addition, 150-micron thick lamination sheets were applied to cover the device as a protective layer from environmental moisture, and the assembly was encapsulated using a heat press at 140°C.

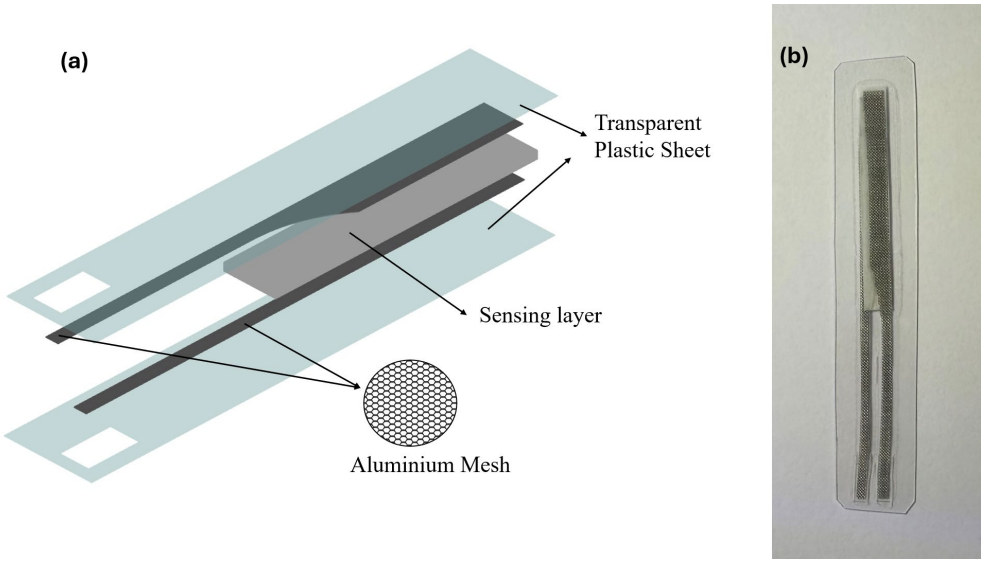

Figure 2. (a) Device schematic, (b) an image of fabricated bending sensor

The thickness of the SC film synthesized for application purposes was measured using an upright microscope (Olympus BX43 microscope). The electrical signal response from the sensor was evaluated using a source meter (Keithley 2410) in the resistance measurement mode. The fabricated bending sensor was tested with varying bending radii of 5, 7.5, 10, and 12.5 mm. A lab-made 360° rotating cam coupled with a motor was used as the external force source for repetitive bending tests of the device.

3. Results and Discussion

Figure 3 depicts the XRD spectra of the prepared R-ZnO at 3, 5, and 10-h reaction times defined as Z-3, Z-5, and Z-10, respectively. The dominant diffraction peak was observed at the orientation plane of the hexagonal structure zinc oxide. The diffraction peaks at a diffraction angle of 30°- 65° were (100), (002), (101), (102), (110), and (103), which corresponded with the JCPDS No.01-080-0075 polycrystalline ZnO (Ejsmont & Goscianska, 2023). All samples displayed a high crystallinity and high phase purity of prepared ZnO. The dominant peaks corresponded to the (100), (002), and (101) planes, of which the (101) plane was the preferred one (Katiyar et al., 2020). The orientation of the (101) plane was parallel to the base substrate, which showed that it could be used to create a suitable device for measuring curvature.

The crystalline parameters, such as crystalline size (D) and the effective strain in the prepared R-ZnO was estimated using the Williamson-Hall analysis shown below (Keawkusonwiwat et al., 2023).

$$\beta \cos\theta = \left(\frac{K\lambda}{D}\right) + 4\varepsilon_{micro} \sin\theta \quad (1)$$

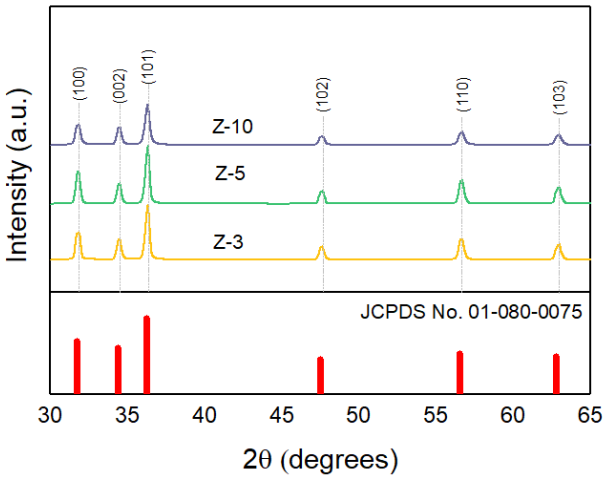

Figure 3. XRD spectra of R-ZnO at different hydrothermal reaction times

Where D is the crystalline size, β is the full width at half-maximum of diffraction peak, θ is the diffraction angle, λ is the wavelength of the X-ray source (Cuκα), K is a constant (0.89), and ε_{micro} is the effective strain of prepared samples. Thus, the average crystalline size and strain of R-ZnO can be performed with the slope and the y-axis interception of the βcosθ-4sinθ relation.

In addition, the dislocation density (δ) of R-ZnO was calculated from the Williamson and Smallman relation, which is the length of dislocation lines per unit volume of grain size as seen in the following equation (Keawkusonwiwat et al., 2023).

$$\delta = \frac{1}{D^2} \tag{2}$$

The calculated crystal structure parameters are shown in Table 1. The grain size increased while the dislocation density and strain decreased with an increase in the reaction times of the hydrothermal process. The compressive strain in the prepared R-ZnO was represented by a negative sign of the strain value. Usually, the compression strain is the deformation along a line segment that decreases in length when a load is applied. In the hydrothermal process, the reaction times revealed the decrease of the lattice imperfections, which improved the microstructure, defect, size, and shape of nanomaterials (Wasly et al., 2018).

A larger grain size indicates extensive crystal coalescence and low grain boundaries, correlating directly with reduced defect sites in the crystal structure of the R-ZnO. The reduction in the effective strain demonstrated that longer hydrothermal growth time relieved the crystal structure distortion, including the healing of defects and internal stress in the R-ZnO. Decreasing dislocation density with the prolonged hydrothermal process confirmed the reduction in crystalline defect density. Thus, the results indicated that the prolonged hydrothermal reaction time promoted the growth of more perfect ZnO crystals with lower defects in crystalline (Kale et al., 2014; Holi et al., 2016; Wasly et al., 2018).

Table 1. Physical parameters of synthesized R-ZnO at different hydrothermal times

Hydrothermal Times (hrs.)	Grain Size (nm.)	Microstrain (ε_{micro}) x10^{-3}	Dislocation Density (δ) x10^{15} (line/m^2)	Rods Length (μm)	Rods Diameter (nm)	Aspect ratio (Rods length/Rods Diameter)	Optical Energy Band Gap (eV)
3	16.36	-2.51	3.73	6.19	469.04	13.19	3.29
5	20.48	-1.27	2.38	6.65	471.27	14.11	3.30
10	22.11	-0.41	2.04	10.16	906.15	11.21	3.32

Generally, Raman spectra can provide information about vibration modes corresponding to the chemical bonding in materials. This technique can be used to identify the quality of the material. Figure 4 shows the Raman spectra of R-ZnO produced at different reaction times. Several bands of Raman active phonon mode of hexagonal ZnO were observed. The strong peak was located at a wavenumber of 441 cm$^{-1,}$ corresponding to E_2^{high} mode. It is related to the hexagonal wurtzite structure of prepared R-ZnO. In addition, the weak peaks at 541 and 585 cm^{-1} were ascribed to the E_1^{low} mode and the second order $2B_1^{low}$; 2LA overtones (Vinod et al., 2012). These are associated with structure disorders of ZnO, such as Zn interstitial and oxygen vacancy. Other weak peaks were found at 334 and 382 cm^{-1} wavenumbers and defined as the multiple phonon scattering modes of E_2^{high} - E_2^{low} and A_1(TO), respectively. The characteristics of the Raman spectrum of E_2^{high} and E_1^{low} modes indicated the highly high-quality crystallinity of the prepared R-ZnO with hexagonal wurtzite structure. The intensity of the E_2^{high} mode remained a dominant peak, while the peaks indicating disorder modes, including E_2^{high}–E_2^{low}, A_1(TO), $2B_1^{low}$, etc., were of lower intensity. This further highlighted the effects of lengthening the hydrothermal process on crystal growth (Zhang et al., 2012). Moreover, this phenomenon was consistent with the XRD results.

The morphologies of the prepared R-ZnO were observed by SEM, as shown in Figure 5. The rod length and rod diameter of the R-ZnO were directly estimated from the SEM images, as shown in the inset of Figure 5. The values of the rod length and rod diameter of the R-ZnO are presented in Table 1. The rod-like structure can be seen with variations in rod length and rod diameter. The rod length and diameters of the R-ZnO increased with hydrothermal time. In other reports, the effects of the addition of precursor material in the hydrothermal process were observed in the shape and morphology of prepared R-ZnO (Holi et al., 2016). In addition, the aspect ratio of R-ZnO was evaluated based on the rod length and rod diameter of R-ZnO, as shown in Table 1.

The optical reflection method was applied to examine the optical band gap of prepared R-ZnO. Figure 6 depicts the room-temperature UV-VIS reflectance spectra of the R-ZnO. The edge of reflectance spectra was in the UV region of 350-400 nm. The optical band gap of the sample was calculated using the Kubelka-Munk equation (Poornaprakash et al., 2021; Limthin et al., 2023).

$$F(R) = \frac{(1-R)^2}{2R} \tag{3}$$

The optical band gap can be estimated as follows (Poornaprakash et al., 2021).

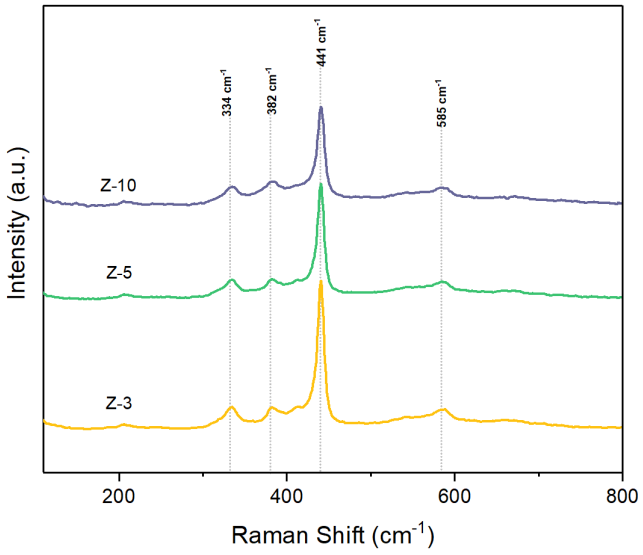

Figure 4. Raman spectra of R-ZnO at different reaction times

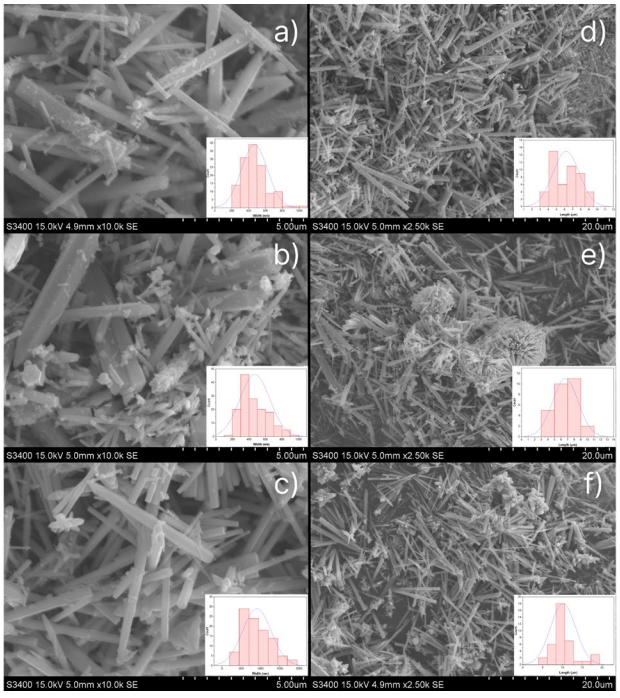

Figure 5. Morphological images at high magnification of prepared R-ZnO at different reaction times: (a) Z-3, (b) Z-5, (c) Z-10, and morphologies images at low magnification of (d) Z-3, (e) Z-5, and (f) Z-10, respectively. The distribution graphs of R-ZnO in the inset images (a), (b), (c) are the rod diameter distribution, and (d), (e), and (f) are the rod length distribution.

$$(F(R)hv)^{p} = A(hv - E_g) \quad (4)$$

Where E_g is the optical energy bandgap, hν is the incident optical energy, A is a constant, and p is a value of 2 for direct band gap material. The value of the optical band gap can be estimated from the extrapolation of the linear portion of the optical energy bandgap, as shown in the inset of Figure 6. The optical energy band gaps of prepared R-ZnO were obtained in the 3.29 - 3.32 eV range, depending on the hydrothermal reaction times as shown in Table 1. Those values were smaller than the bulk ZnO (3.37 eV), which might result from the effect of the redshift phenomenon (Li et al., 2018).

The viscosity characteristics of the R-ZnO and starch composite solution were evaluated as shown in Figure 7. The relationship between viscosity and shear stress to shear rates is demonstrated in Figure 7a. All composite solutions exhibited a decreased viscosity with increasing shear rate, which exponentially decreased. Meanwhile, the shear stress increased with the increasing shear rate. This characteristic is a behavior of shear thinning (Soleimani-gorgani, 2015). Those properties impacted the preparation of uniform thin films with the solution process. These influenced the sensing properties of flexible devices, which can maintain physical shape under stress. Before fabricating the bending sensor device, FTIR analysis was used to determine the compounds and functional groups formed in the prepared SC films. The composite films of starch and 1%wt. of R-ZnO at reaction times of 3, 5, and 10 h were defined as SC 1% wt. Z-3, SC 1% wt. Z-5, and SC 1% wt. Z-10, respectively. Figure 8 exhibits the FTIR spectra in the wavenumber range between 480 to 4,000 cm^{-1}. The FTIR spectra show strong absorption at 3,266 cm^{-1} (O-H stretching), 2,884 cm^{-1} (C-H stretching), 1,630 cm^{-1} (C=O stretching), and 1,410 cm^{-1} (C-O stretching). In addition, the absorption at 1,007 cm^{-1} corresponds to the O-H stretching of glycerol used as a plasticizer in pristine starch films. The changing position and intensity of the infrared absorption peaks of SC films might be due to the incorporation of R-ZnO into the SC films, which involved chemical reactions between the filler nanomaterial and starch matrix components (Kumar et al., 2020). In other work (Di et al., 2021; Gautam et al., 2021; Shapi'i et al., 2022), FTIR analysis demonstrated strong hydrogen bonding interactions between the hydroxyl groups on the starch matrix and the surface hydroxyl groups on the R-ZnO. These strong bonds created a stable and continuous interfacial network that firmly anchored the R-ZnO within the starch matrix, effectively preventing structural detachment even under repeated mechanical deformation.

The sensing behavior of the pristine starch films and SC R-ZnO fabricated bending device was performed, and the measurement setup is shown in Figure 9a. A 3D printing machine printed the curvature slot of the difference bending radius. The device was bent, and electrical resistance was measured with a precision source meter (Keithley 2410). The sensitivity of bending devices can be estimated from Park and Lee (2021).

$$S = \frac{\Delta R}{R_0} \times 100\% \quad (5)$$

Where ΔR is the change in resistance between bent and unbent or flat resistance, R_0 is the initial resistance of flat condition. The sensitivity (S) of the bending device is a parameter that demonstrates the device's response when a bending force is applied. It was calculated as the percentage change in resistance ($\Delta R/R_0$) from the initial resistance R_0.

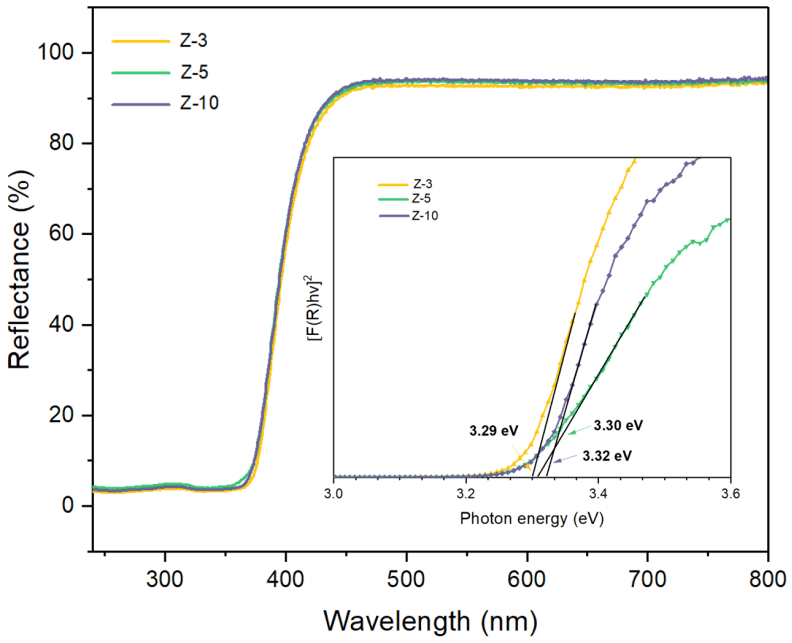

Figure 6. Tauc plot of prepared R-ZnO at different reaction times

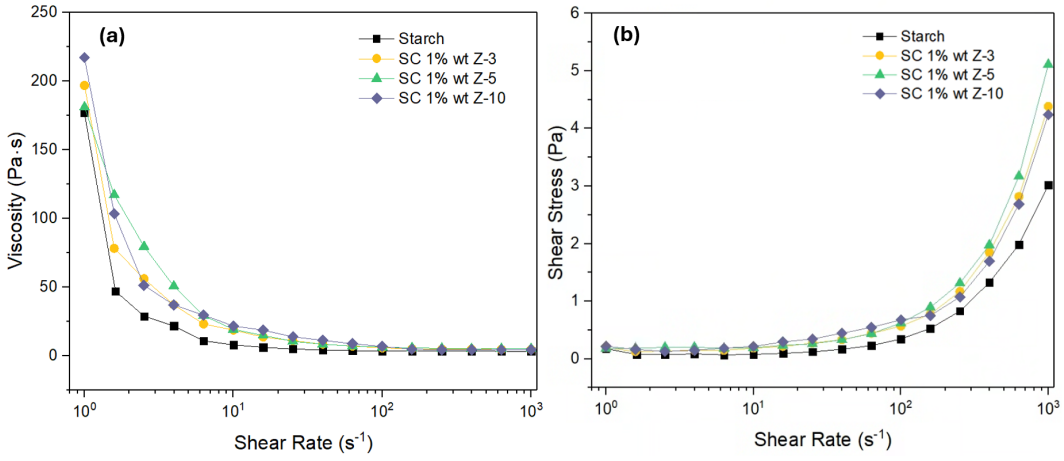

Figure 7. (a) Viscosity and (b) shear stress characteristics of R-ZnO and starch composite solution

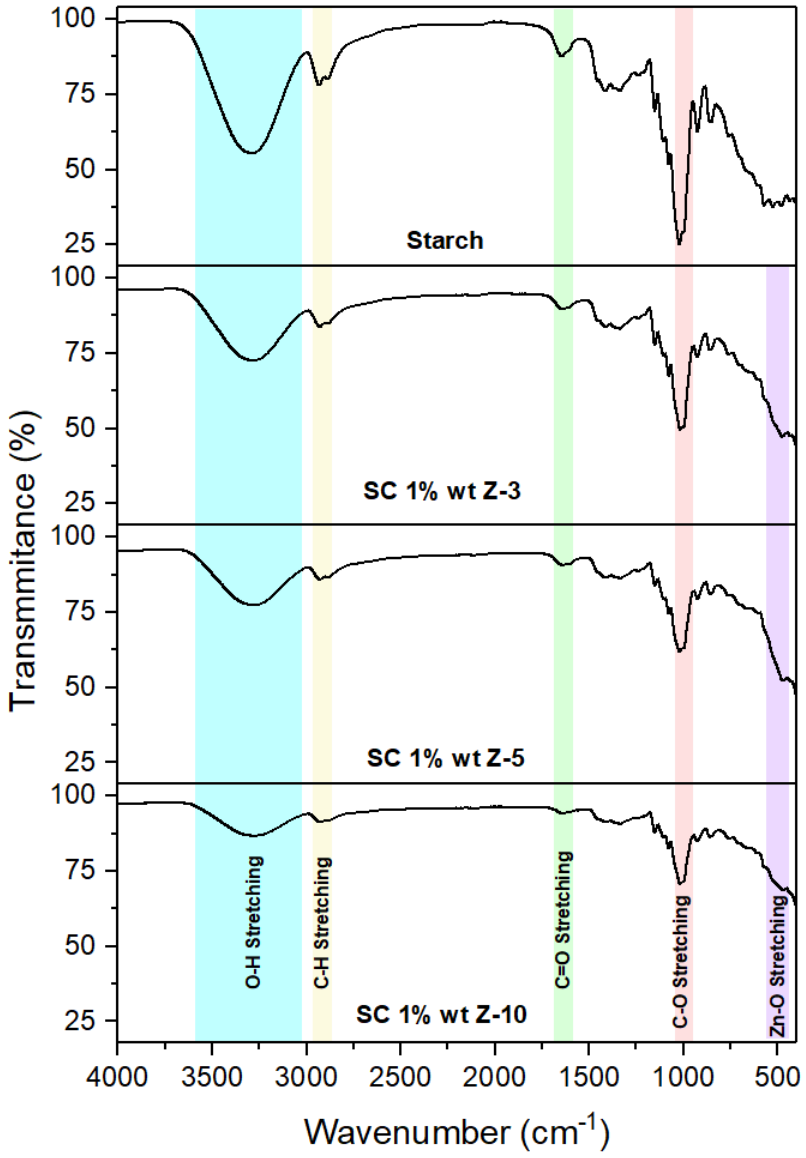

Figure 8. FTIR spectra of pristine starch film and SC R-ZnO films

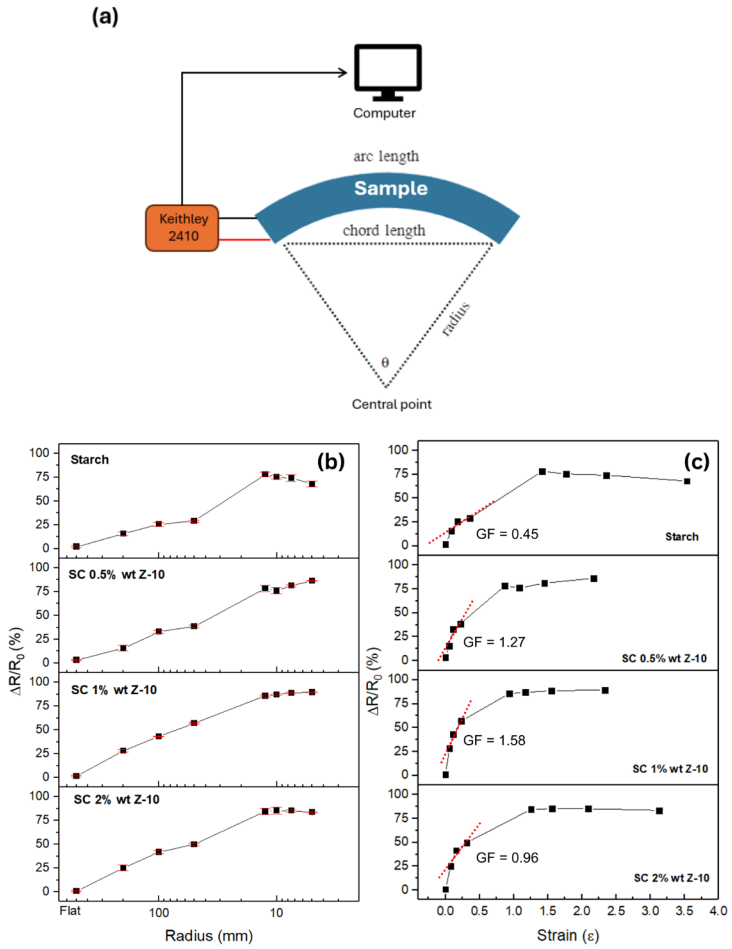

Figure 9. (a) The bending test system using a 3D printed device that determines the curvature radius based on the sensor bending, (b) $\Delta R/R_0$ sensing characteristics, and (c) the gauge factor characteristics of the devices at various concentrations of R-ZnO in SC films (red dot line as the trend line for GF calculations).

In addition, the strain of the bending device during bending measurement can be achieved (Deka et al., 2022).

$$\varepsilon = \frac{t}{2r} \tag{6}$$

Where t is the device's thickness and r is the radius of curvature. This equation shows the inverse relationship between strain and the radius of curvature, with a smaller radius of curvature resulting in a higher strain value.

Moreover, the gauge factor (GF) of the bending device can be calculated from Wang et al. (2023).

$$GF = \frac{(\frac{\Delta R}{R_0})}{\varepsilon} \quad (7)$$

The gauge factor (GF) is a dimensionless quantity that describes the sensitivity of a bending device to applied strain. It is defined as the ratio of the relative change in resistance ($\Delta R/R_0$) to the applied strain (ε). Usually, a higher value of GF indicates a more significant change in resistance for applied strain.

Figure 9b depicts the relative change in resistance ($\Delta R/R_0$) of the fabricated devices at various concentrations of 0.5 %wt. to 2 %wt. for 10-h processed R-ZnO, which are defined as SC 0.5% wt. Z-10, SC 1% wt. Z-10, and SC 2% wt. Z-10, respectively. The change in device resistance might be due to the influence of solid physical contact of R-ZnO during bending measurement. The pathway of charge current in the device was changed when subjected to either tensile or compressive states. The maximum sensitivity of devices at concentrations of R-ZnO at 0.5, 1, and 2 %wt. was 86.4%, 89.5%, and 83.5%, respectively. In the case of pristine starch film, the maximum sensitivity was 78.1%. Figure 9c demonstrates the relationship between strain and the change of resistance ($\Delta R/R_0$) of the fabricated devices at various concentrations of 0.5 %wt. to 2 %wt. for the 10-h R-ZnO. The maximum GF values of the devices at concentrations of R-ZnO 0.5, 1, and 2 % were 1.27, 1.58, and 0.96, respectively. The pristine starch films demonstrate a maximum GF value of 0.45. The device that had a concentration of 1 %wt. of R-ZnO exhibited the optimal values of the bending devices. The optimized concentration of R-ZnO was observed at 1%wt. This might be the effect of rod-like structures that formed a continuous percolative network path, which improved the charge transport process in the composite film (Ponnamma et al., 2019; Kesler et al., 2023). Moreover, the composite of R-ZnO with starch film can enhance the flexibility of film production. In this case, the effect of morphology of rod-like structures was performed with higher sensitivity with respect to higher rod length and rod diameter. Therefore, the R-ZnO processed with 10 h shows the highest sensitivity value (Lei et al., 2024). Therefore, the condition of 1 % wt. R-ZnO was later used to prepare the bending device.

Figure 10a depicts the sensitivity of bending devices of the SC film. The composite films of starch and 1%wt. of R-ZnO prepared at hydrothermal reaction times of 3, 5, and 10 h were defined as SC 1% wt. Z-3, SC 1% wt. Z-5, and SC 1% wt. Z-10, respectively. The maximum sensitivity of the SC 1% wt. Z-3, SC 1% wt. Z-5, and SC 1% wt. Z-10 devices were 80.3%, 88.3%, and 89.5%, respectively. The GF values of SC 1% wt. Z-3, SC 1% wt. Z-5, and SC 1% wt. Z-10 devices were 1.57, 1.29, and 1.58, respectively. The maximum sensitivity was observed at the condition of 10 h R-ZnO. This might be because of the influence of the shape and size of the nanorods, which affected the sensing behavior of bending devices. As shown in Table 2, the R-ZnO 10 h sample exhibited the highest rod length and rod diameter. Muhammad and Kim (2023) reported on the effect of the bending direction of flexible ZnO nanorod bending sensors. The electrical current through the unbent and bent states was also decreased with convex bending direction. In addition, Zhu et al. (2022) reported the influence of the microstructure of ZnO nanorods on the sensitivity of flexible tactile sensors. Larger ZnO nanorods exhibited higher sensitivity due to the effect of the c-axis orientation.

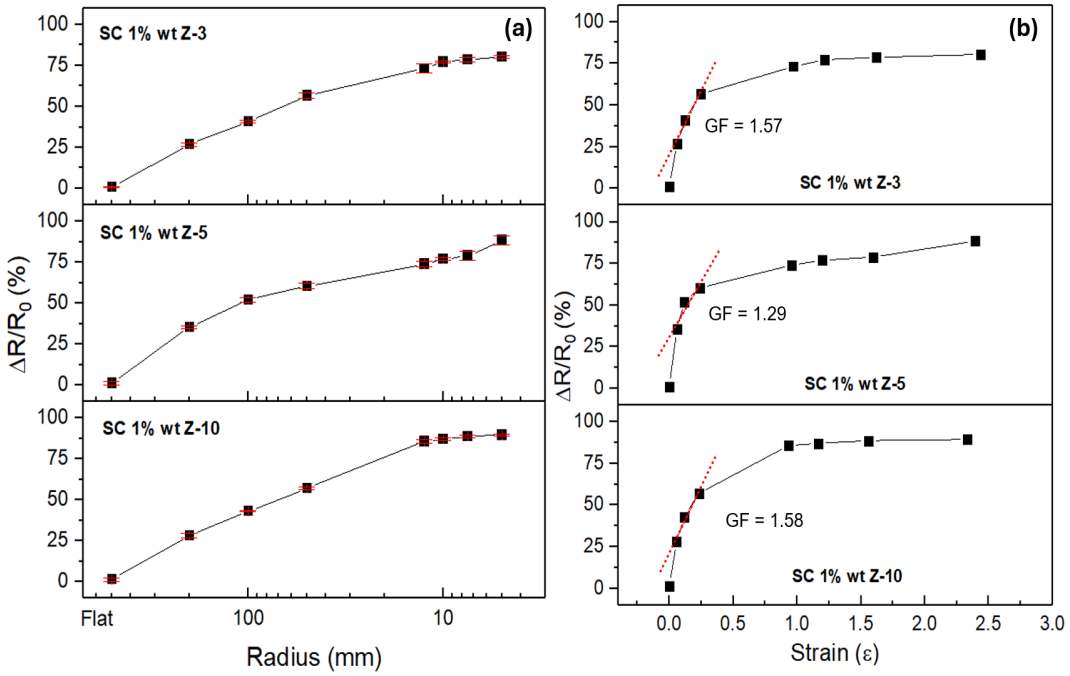

Figure 10. (a) $\Delta R/R_0$ sensing characteristics, and (b) the gauge factor characteristics of the fabricated bending device with R-ZnO samples at different hydrothermal times of 3, 5, and 10 h. (red dot line as the trend line for GF calculations)

Usually, the sensitivity of the bending device based on composite film depends on the crystallinity of the filler that facilitates the charge transfer in the composite sensing layer. With high crystalline, a large grain size with a low grain boundary is presented; thus, high sensitivity is contributed. In addition, the network connectivity of filler in the starch matrix is one of the key parameters. The R-ZnO with long rod length enhances the inter-rod connection area and strengthens the percolative conductive network within the starch film. This improved connectivity yields more pronounced resistance changes upon bending, raising sensitivity. In the case of GF values, the GF depends primarily on the efficiency of strain transfer from the starch matrix to the R-ZnO network, which is dependent on the geometry of R-ZnO, such as shape, aspect ratio resulting in its lowest GF of R-ZnO 5 h and highest GF values at R-ZnO 10 h (Amjadi et al., 2016; Tan et al., 2022).

The repeatability of a bending devices is a key characteristic of the device. Figure 11a shows the setup for repeatability measurement. A rotating circle dish with an off-axis central point was used as the actuator for pressing and releasing the device to perform a bending cycle at a bending radius of 200 mm. The rotating dish was coupled with a stepping motor to control the actuator at half a revolution per second. The system was controlled by a microcontroller via computer interfacing. Figure 11b demonstrates the relative change in resistance ($\Delta R/R_0$) of the fabricated devices and pressed cycles. The inset of Figure 11b shows the resistance behavior during measurement cycles. After 1,600 test cycles, the fabricated devices still responded well to bending sensing.

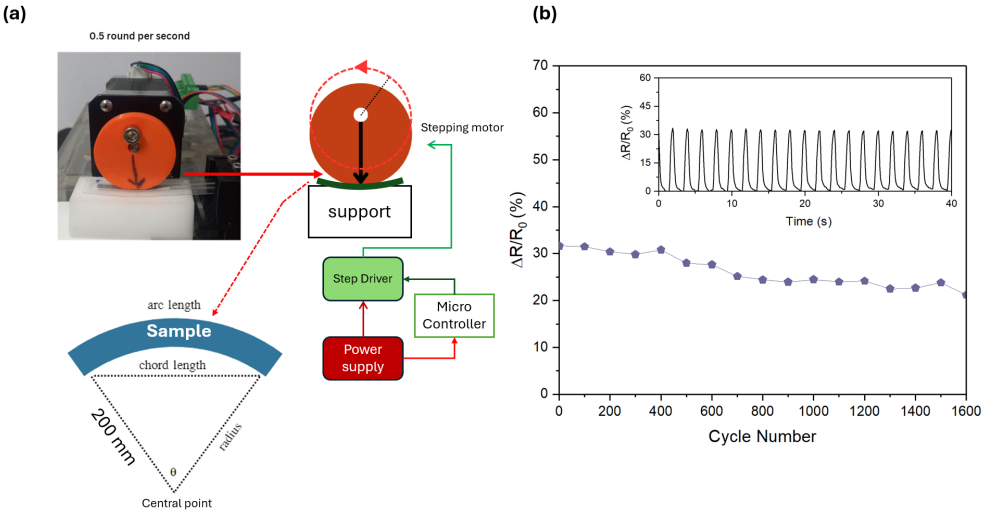

Figure 11. (a) Durability testing system using a rotating plastic cam, (b) the repeatability test of fabricated device, and the inset shows the sample characteristics of device response cycles

Figures 12(a)-(c) depicts the fabricated device attached to the robotic hand. The robotic hand was made from the 3D print process with motion control by a servo motor. On the robotic hand, dual sensors were attached to define the first (1st) and second (2nd) finger joints, as shown in Figure 12(a). The states of the robotic hand were controlled between default or flat state and robotic finger flexion state, as shown in Figure 12(b)-(c). The computer was used to control the robotic hand motion and record signal readout. Figure 12(d) demonstrates the signal from both sensors with 10 cycle repetitions in 10 s of each cycle. The devices were responsible for sensing with good stability of all cycles. In addition, the response and recovery times of the fabricated device were achieved from a transition time of 10% to 90% and 90% to 10% of the sensor signal, as shown in Figure 12(c), which were 0.23 s and 0.15 s for the response and recovery times. These response time values are relatively fast for practical use. In addition, the hysteresis loop characteristic of the device was demonstrated. The hysteresis of the bending sensor (H_s) was obtained by the following equation (Li et al., 2020).

$$H_S = \frac{\left|R_{up} - R_{down}\right|_{\max}}{R_{\max} - R_{\min}} \times 100\% \quad (8)$$

Where $\left|R_{up} - R_{down}\right|_{max}$ is the maximum difference in resistance values at the exact bending radius of flat state to bending state (defined as Bending) and bending state to flat state (defined as Release), R_{max} and R_{min} are the highest and lowest resistances. This relation might be the effect of imperfect behavior at various bending states. Figure 12(f) depicts the hysteresis error versus bending radius. The hysteresis error of all bending radii is less than 5 %, indicating the good performance of the fabricated device. The optimum device showed the maximum hysteresis of 4.81% at a bending radius of 60 mm.

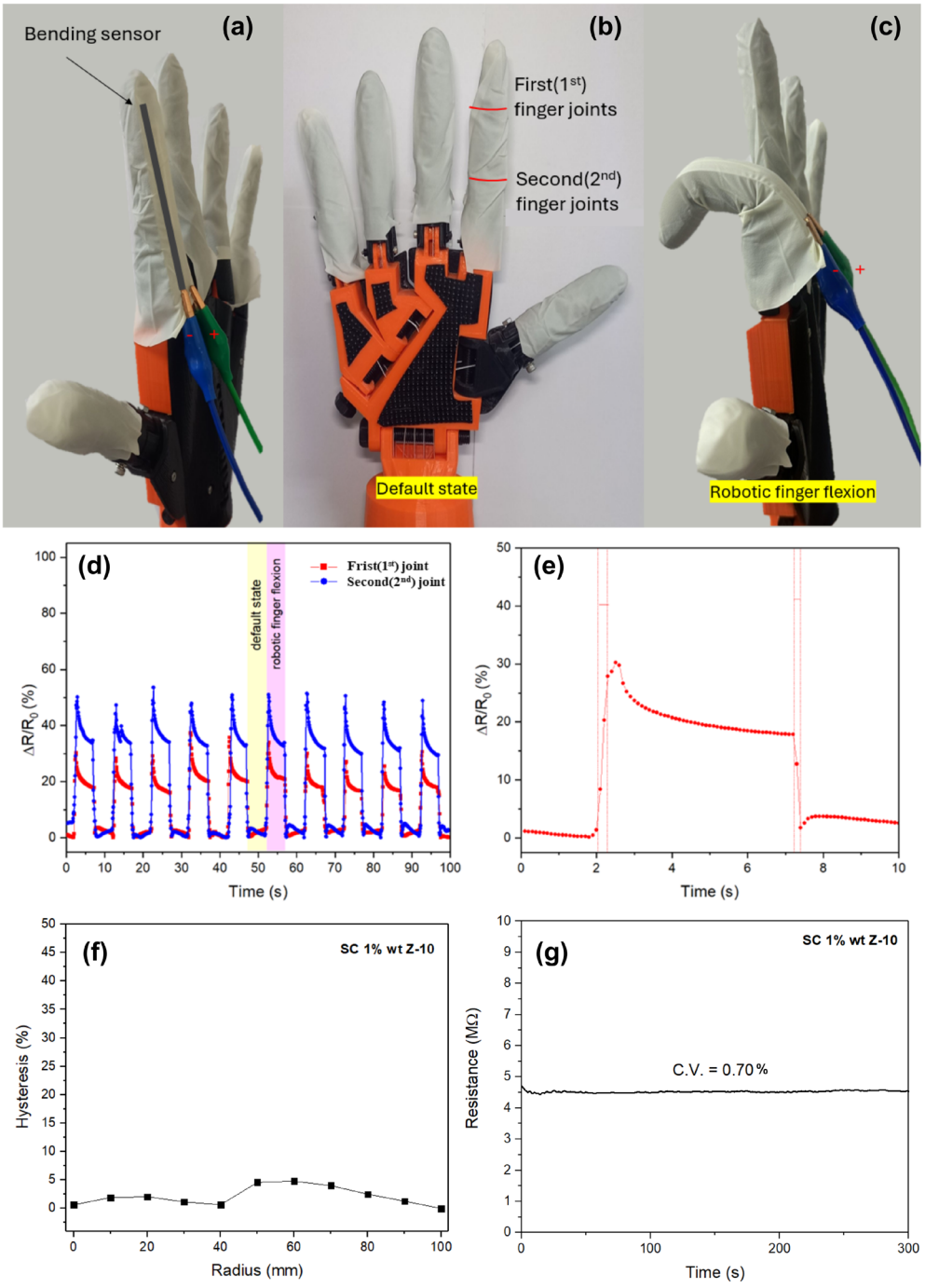

Figure 12. (a)-(c) Actual device attached to the robotic hand with computer control, (d) the signal from the fabricated device connected to the robotic hand, (e) the response and recovery times of the actual device attached to the robotic hand, (f) long-term stability, and (g) the hysteresis characteristic of the device

The long-term stability of the device was achieved by measuring the device in a fixed flat position for a duration of 300 s, as shown in Figure 12(g). The stability of the device was calculated in terms of the coefficient of variation (CV) as follows (Keawkusonwiwat et al., 2023).

$$CV = \frac{\sigma}{\mu} \times 100 \quad (9)$$

Where σ and μ are the standard deviation and mean of the time-series data. The CV of SC 1% Z-10 device was 0.70%. That indicated good stability in the long-term for flexible device applications.

Table 2 demonstrates the performance comparison of fabricated bending/flexible sensors with other works. The selected comparison works are based on resistive sensing measurements with various materials. Laser-induced graphene (LIG)-base sensors (Barja et al., 2024) demonstrate high gauge factors, indicating significant strain sensitivity. The change in resistance was caused by the piezoresistive effect of laser-induced graphene (LIG), which was transferred from a polyimide (PI) sheet to a highly flexible PDMS (polydimethylsiloxane) substrate. When the material underwent tensile strain or bending, the LIG porous and interconnected graphene structure deformed, which changed electrical resistance. In the case of MXene $Ti_3C_2T_X$ on paper (Bu et al., 2021), the change in resistance was caused by the microcrack structure in the conductive layer. Under tensile or torsional stress applied to the device, the MXene structure opened and closed according to the deformation in the material, leading to changes in the conductive network and electrical resistance. For the PDMS/carbon black (CB) (Wang et al., 2023), the porous structure was formed through the use of a deep eutectic solvent, which induced phase separation between CB and PDMS materials. This affected the porous conductive network in the device. When the material bent, this conductive network was either compressed or stretched, leading to changes in electrical resistance. In our work, the sensor of SC with R-ZnO demonstrated a well-balanced performance with high sensitivity (89.5%), fast response/recovery times (0.23/0.15 s), and durability over 1,600 test cycles. The R-ZnO contributed to both the mechanical reinforcement of the starch matrix and the enhancement of piezoresistive properties, making the composite sensor highly responsive to bending strain. In the practical application of a fabricated bending measurement device, the performance of the device depends on the response mechanism that provides high output signal value, response sensitivity, and a good GF value. The mechanism depends on the properties of the composite material related to the mixture of both starch as the host matrix and R-ZnO as the filler to produce the bending response. Furthermore, the performance of the fabricated device depends on the structure of the synthesized R-ZnO. The rod-like morphology of R-ZnO directly affected the efficient distribution of mechanical stress throughout the composite film. This stress distribution preserved the composite mechanical integrity and electrical connectivity even after many bending cycles. In addition, the influence of surface hydroxyl groups bonding on the R-ZnO and bonding with starch chains, which enhanced interfacial adhesion (Di et al., 2021; Gautam et al., 2021; Shapi'i et al., 2022), promoted the effective transfer of bending-induced stresses from the starch to the R-ZnO. Therefore, the delamination or internal crack growth was reduced, and the output signal was stabilized. Combining the bending characteristics and high repeatability improves its performance for wearable electronic devices.

Table 2. Comparison of bending sensor performances

Materials	Sensitivity (formula)	Response/ Recovery time (s)	Repeatability Cycle (n)	Gauge Factor	Ref.
a LIG: PDMS	4.31 (R/R_0)	1.040/-	1,500	111	(Barja et al., 2024)
$Ti_3C_2T_X$ MXene/paper	~11 ($\Delta R/R_0$ x100%)	0.2/0.2	1,000	3.9	(Bu et al., 2021)
a Porous PDMS/CB	~25 ($\Delta R/R_0$ x100%)	0.3/0.18	10,000	45.6	(Wang et al., 2023)
R-ZnO: Starch	89.5 ($\Delta R/R_0$ x100%)	0.23/0.15	1,600	1.58	This Work

4. Conclusions

The starch and R-ZnO composite films were prepared for bending sensors. The R-ZnO was synthesized by hydrothermal processes with various hydrothermal times of 3, 5, and 10 h. The morphologies of prepared ZnO confirmed the rod-like structure, with the physical properties of R-ZnO depending on the hydrothermal times. It was found that the SC film of 1%wt. R-ZnO at a hydrothermal reaction time of 10 h demonstrated a high sensitivity at 89.5% with a gauge factor of 1.58. In addition, the 1%wt. R-ZnO at 10-h SC film exhibited fast response/recovery times at 0.23/0.15 s with high stability of bending cycles of more than 1,600 cycles. The application of the fabricated devices as sensing devices for a robotic hand were demonstrated. Therefore, the SC films of R-ZnO and natural starch can be considered as suitable candidates for potential bending devices.

5. Acknowledgements

The authors acknowledge the facilities, and technical assistance from Nanotechnology and Materials Analytical Instrument Service Unit (NMIS) of School of Integrated Innovative Technology, King Mongkut Institute of Technology Ladkrabang.

6. Authors' Contributions

Kitikamol Feemuchang: Writing-review & editing, Methodology, Investigation. Korakot Onlaor: Formal analysis, Conceptualization, Supervision. Benchapol Tunhoo: Writing-review & editing, Methodology, Validation. Thiwawong Thiwawong: Methodology, Validation, Supervision

7. Conflicts of Interest

The authors declare no conflict of interest.

ORCID

Korakot Onlaor https://orcid.org/0000-0001-5534-4992

Benchapol Tunhoo https://orcid.org/0000-0003-4277-7670

Thiwawong Thiwawong https://orcid.org/0000-0001-9302-0585

References

Apandi, N. A. A., Razak, N. A. S. A., Masri, M., Yusoff, S. F., & Lazim, A. M. (2013). A preliminary study on gum arabic as a binder in preparation of starch based edible plastic. *International Journal on Advanced Science, Engineering and Information Technology*, 3(2), 148-150. https://doi.org/10.18517/ijaseit.3.2.301

Amjadi, M., Kyung, K.-U., Park, I., & Sitti, M. (2016). Stretchable, skin-mountable, and wearable strain sensors and their potential applications: A review. *Advanced Functional Materials*, 26(11), 1678-1698. https://doi.org/10.1002/adfm.201504755

Amjadi, M., Pichitpajongkit, A., Lee, S., Ryu, S., & Park, I. (2014). Highly stretchable and sensitive strain sensor based on silver nanowire–elastomer nanocomposite. *ACS Nano*, 8(5), 5154-5163.

Arifin, H., Nurhadi, B., Azlin-Hasim, S., Masruchin, N., Vania, P., & Hilmi, A. (2022). Corn starch-based bionanocomposite film reinforced with ZnO nanoparticles and different types of plasticizers. *Frontiers in Sustainable Food Systems*, 6, Article 886219. https://doi.org/10.3389/fsufs.2022.886219

Azmi, Z. H., Mohd Aris, S. N., Abubakar, S., Sagadevan, S., Siburian, R., & Paiman, S. (2022). Effect of seed layer on the growth of zinc oxide nanowires by chemical bath deposition method. *Coatings*, 12(4), Article 474. https://doi.org/10.3390/coatings12040474

Barja, A. M., Ryu, Y. K., Tarancon, S., Tejado, E., Hamada, A., Velasco, A., & Martinez, J. (2024). Laser-Induced graphene strain sensors for body movement monitoring. *ACS Omega*, 9(37), 38359-38370. https://doi.org/10.1021/acsomega.3c09067

Bu, Y., Shen, T., Yang, W., Yang, S., Zhao, Y., Liu, H., Zheng, Y., Liu, C., & Shen, C. (2021). Ultrasensitive strain sensor based on superhydrophobic microcracked conductive Ti3C2Tx MXene/paper for human-motion monitoring and E-skin. *Science Bulletin*, *66*(18), 1849-1857. https://doi.org/https://doi.org/10.1016/j.scib.2021.04.041

Costa, J. C., Spina, F., Lugoda, P., Garcia-Garcia, L., Roggen, D., & Münzenrieder, N. (2019). Flexible sensors—from materials to applications. *Technologies*, 7(2), Article 35. https://doi.org/10.3390/technologies7020035

Deka, N., Bera, A., Roy, D., & De, P. (2022). Methyl methacrylate-based copolymers: Recent developments in the areas of transparent and stretchable active matrices. *ACS Omega*, 7(42), 36929-36944. https://doi.org/10.1021/acsomega.2c04564

Di, X., Ma, Q., Xu, Y., Yang, M., Wu, G., & Sun, P. (2021). High-performance ionic conductive poly(vinyl alcohol) hydrogels for flexible strain sensors based on a universal soaking strategy. *Materials Chemistry Frontiers*, 5, 315-323. https://doi.org/10.1039/D0QM00625D

Ejsmont, A., & Goscianska, J. (2023). Hydrothermal synthesis of ZnO superstructures with controlled morphology via temperature and pH optimization. *Materials*, 16(4), Article 1641. https://doi.org/10.3390/ma16041641

Ferreira, A., Silva, J. P., Rodrigues, R., Martin, N., Lanceros-Méndez, S., & Vaz, F. (2019). High performance piezoresistive response of nanostructured ZnO/Ag thin films for pressure sensing applications. *Thin Solid Films*, 691, Article 137587. https://doi.org/https://doi.org/10.1016/j.tsf.2019.137587

Gautam, N., Garg, S., & Yadav, S. (2021). Underutilized finger millet crop for starch extraction, characterization, and utilization in the development of flexible thin film. *Journal of Food Science and Technology*, 58(11), 4411-4419. https://doi.org/10.1007/s13197-020-04926-0

Guzenko, N., Godzierz, M., Kurtyka, K., Hercog, A., Nocoń-Szmajda, K., Gawron, A., Szeluga, U., Trzebicka, B., Yang, R., & Rümmeli, M. H. (2023). Flexible piezoresistive polystyrene composite sensors filled with hollow 3D graphitic shells. *Polymers*, 15(24), Article 4674. https://doi.org/10.3390/polym15244674

Holi, A. M., Zainal, Z., Talib, Z. A., Lim, H.-N., Yap, C.-C., Chang, S.-K., & Ayal, A. K. (2016). Effect of hydrothermal growth time on ZnO nanorod arrays photoelectrode performance. *Optik*, 127(23), 11111-11118. https://doi.org/10.1016/j.ijleo.2016.09.015

Joongpun, P., Feemuchang, K., Onlaor, K., Thiwawong, T., & Tunhoo, B. (2024). Facile synthesis of zinc oxide nanorods using a single-phase flow with 3D printed device. *Thai Journal of Nanoscience and Nanotechnology*, 9(1), 9-18.

Kale, R. B., Hsu, Y.-J., Lin, Y.-F., & Lu, S.-Y. (2014). Hydrothermal synthesis, characterizations and photoluminescence study of single crystalline hexagonal ZnO nanorods with three dimensional flowerlike microstructures. *Superlattices and Microstructures*, 69, 239-252. https://doi.org/10.1016/j.spmi.2014.03.003

Katiyar, A., Kumar, N., Shukla, R. K., & Srivastava, A. (2020). Substrate free ultrasonic-assisted hydrothermal growth of ZnO nanoflowers at low temperature. *SN Applied Sciences*, 2(8), Article 1386. https://doi.org/10.1007/s42452-020-3186-1

Keawkusonwiwat, S., Tunhoo, B., Onlaor, K., & Thiwawong, T. (2023). Preparation of pH sensor based on extended-gate field-effect transistor with spinel ZnCo2O4 thin films by electrostatic spray deposition. *Journal of Electronic Materials*, 52(12), 8095-8107. https://doi.org/10.1007/s11664-023-10736-9

Kesler, D., Ariyawansa, B. P., & Rathnayake, H. (2023). Mechanical properties and synergistic interfacial interactions of ZnO nanorod-reinforced polyamide–imide composites. *Polymers*, 15(6), Article 1522. https://doi.org/10.3390/polym15061522

Khai, T. V., Long, L. N., Khoi, N. H. T., & Thang, N. H. (2022). Effects of hydrothermal reaction time on the structure and optical properties of ZnO/graphene oxide nanocomposites. *Crystals*, 12(12), Article 1825. https://doi.org/10.3390/cryst12121825

Kumar, S., Mudai, A., Roy, B., Basumatary, I. B., Mukherjee, A., & Dutta, J. (2020). Biodegradable hybrid nanocomposite of chitosan/gelatin and green synthesized zinc oxide nanoparticles for food packaging. *Foods*, 9(9), Article 1143. https://doi.org/10.3390/foods9091143

Li, K., Wei, Z., Zhu, X., Zhao, W., Zhang, X., & Jiang, J. (2018). Microstructure and optical properties of ZnO nanorods prepared by anodic arc plasma method. *Journal of Applied Biomaterials and Functional Materials*, 16(1S), 105-111. https://doi.org/10.1177/2280800017751492

Li, Q., Wang, Y., Jiang, S., Li, T., Ding, X., Tao, X., & Wang, X. (2020). Investigation into tensile hysteresis of polyurethane-containing textile substrates for coated strain sensors. *Materials and Design*, 188, Article 108451. https://doi.org/10.1016/j.matdes.2019.108451

Limthin, D., Leepheng, P., Tunhoo, B., Onlaor, K., Klamchuen, A., Phromyothin, D., & Thiwawong, T. (2023). Preparation of surface-modified electrode of copper(ii) oxide mixed with the molecularly imprinted polymer for enhancement of melamine detection with photoelectrochemical technique. *RSC Advances*, 13, 14729-14736. https://doi.org/10.1039/D3RA01854G

Ma, J., Zhu, W., Tian, Y., & Wang, Z. (2016). Preparation of zinc oxide-starch nanocomposite and its application on coating. *Nanoscale Research Letters*, 11(1), Article 200. https://doi.org/10.1186/s11671-016-1404-y

Muhammad, W., & Kim, S.-D. (2023). Flexible bending sensors fabricated with interdigitated electrode structures cross-linked by transition metal doped ZnO nanorods. *Chemosensors*, 11(10), Article 529. https://doi.org/10.3390/chemosensors11100529

Park, J., & Lee, J.-H. (2021). Outward- and inward-distinguishable bending sensor with silver nanowires sandwiched between polydimethylsiloxane layers. *AIP Advances*, 11(12), Article 125309. https://doi.org/10.1063/5.0072506

Ponnamma, D., Cabibihan, J.-J., Rajan, M., Pethaiah, S. S., Deshmukh, K., Gogoi, J. P., Pasha, S. K. K., Ahamed, M. B., Krishnegowda, J., Chandrashekar, B. N., Polu, A. R., & Cheng, C. (2019). Synthesis, optimization and applications of ZnO/polymer nanocomposites. *Materials Science and Engineering: C*, 98, 1210-1240. https://doi.org/10.1016/j.msec.2019.01.081

Poornaprakash, B., Subramanyam, K., Vattikuti, S. V. P., Kumar, M., Kim, Y. L., & Mallem, S. P. R. (2021). Room temperature ferromagnetism and enhanced photocatalytic activity of ZnO:Ga nanorods. *Applied Physics A*, 127(1), Article 64. https://doi.org/10.1007/s00339-020-04201-1

Rathod, K. N., Joshi, Z., Dhruv, D., Gadani, K., Boricha, H., Joshi, A. D., Solanki, P. S., & Shah, N. A. (2018). Size effects on electrical properties of chemically grown zinc oxide nanoparticles. *Materials Research Express*, 5(3), Article 035040. https://doi.org/10.1088/2053-1591/aab5ec

Rittenauer, M., Gladis, S., Gastl, M., & Becker, T. (2021). Gelatinization or pasting? The impact of different temperature levels on the saccharification efficiency of barley malt starch. *Foods*, 10(8), Article 1733. https://doi.org/10.3390/foods10081733

Shapi'i, R. A., Othman, S. H., Basha, R. K., & Naim, M. N. (2022). Mechanical, thermal, and barrier properties of starch films incorporated with chitosan nanoparticles. *Nanotechnology Reviews,*11(1), 1464-1477. https://doi.org/10.1515/ntrev-2022-0094

Shitu, I. G., Katibi, K. K., Muhammad, A., Chiromawa, I. M., Tafida, R. A., Amusa, A. A., & Babani, S. (2024). Effects of irradiation time on the structural, elastic, and optical properties of hexagonal (wurtzite) zinc oxide nanoparticle synthesised via microwave-assisted hydrothermal route. *Optical and Quantum Electronics*, 56(2), Article 266. https://doi.org/10.1007/s11082-023-05867-6

Soleimani-gorgani, A. (2015). Inkjet printing. In J. Izdebska & S. Thomas (Eds.). *Printing on polymers: fundamentals and applications* (pp. 231-246). William Andrew.

Song, J., & Lim, S. (2007). Effect of Seed Layer on the Growth of ZnO Nanorods. *The Journal of Physical Chemistry C*, 111(2), 596-600. https://doi.org/10.1021/jp0655017

Spinelli, G., Lamberti, P., Tucci, V., Vertuccio, L., & Guadagno, L. (2018). Experimental and theoretical study on piezoresistive properties of a structural resin reinforced with carbon nanotubes for strain sensing and damage monitoring. *Composites Part B: Engineering*, 145, 90-99. https://doi.org/10.1016/j.compositesb.2018.03.025

Sun, S., Guo, L., Chang, X., Liu, Y., Niu, S., Lei, Y., Liu, T., & Hu, X. (2019). A wearable strain sensor based on the ZnO/graphene nanoplatelets nanocomposite with large linear working range. *Journal of Materials Science*, 54(9), 7048-7061. https://doi.org/10.1007/s10853-019-03354-6

Tan, S. X., Andriyana, A., Ong, H. C., Lim, S., Pang, Y. L., & Ngoh, G. C. (2022). A comprehensive review on the emerging roles of nanofillers and plasticizers towards sustainable starch-based bioplastic fabrication. *Polymers*, 14(4), Article 664. https://doi.org/10.3390/polym14040664

Vieira, M. G. A., da Silva, M. A., dos Santos, L. O., & Beppu, M. M. (2011). Natural-based plasticizers and biopolymer films: A review. *European Polymer Journal*, 47(3), 254-263. https://doi.org/10.1016/j.eurpolymj.2010.12.011

Vinod, R., Sajan, P., Achary, S. R., Tomas, C. M., Muñoz-Sanjosé, V., & Bushiri, M. J. (2012). Enhanced UV emission from ZnO nanoflowers synthesized by the hydrothermal process. *Journal of Physics D: Applied Physics*, 45(42), Article 425103. https://doi.org/10.1088/0022-3727/45/42/425103

Wang, Y.-F., Yoshida, A., Takeda, Y., Sekine, T., Kumaki, D., & Tokito, S. (2023). Printed directional bending sensor with high sensitivity and low hysteresis for human motion detection and soft robotic perception. *Sensors*, 23(11), Article 5041. https://doi.org/10.3390/s23115041

Wasly, H. S., El-sadek, M. S. A., & Henini, M. (2018). Influence of reaction time and synthesis temperature on the physical properties of ZnO nanoparticles synthesized by the hydrothermal method. *Applied Physics A*, 124, Article 76. https://doi.org/10.1007/s00339-017-1482-4

Yahiya, L. Z., Dhahir, M. K., & Mahdi, Z. F. (2020). *Synthesized ZnO nanorod with different range of morphologies using a simple hydrothermal method. AIP conference proceedings*, 2290, Article 030022. https://doi.org10.1063/5.0031634

Yang, T., Xie, D., Li, Z., & Zhu, H. (2017). Recent advances in wearable tactile sensors: Materials, sensing mechanisms, and device performance. *Materials Science and Engineering: R: Reports*, 115, 1-37. https://doi.org/10.1016/j.mser.2017.02.001

Zhang, Y., Ram, M. K., Stefanakos, E. K., & Goswami, D. Y. (2012). Synthesis, characterization, and applications of ZnO nanowires. *Journal of Nanomaterials*, 2012, Article 624520. https://doi.org/10.1155/2012/624520

Zhu, L., Xiang, Y., Liu, Y., Geng, K., Yao, R., & Li, B. (2022). Comparison of piezoelectric responses of flexible tactile sensors based on hydrothermally-grown ZnO nanorods on ZnO seed layers with different thicknesses. *Sensors and Actuators A: Physical*, 341, Article 113552. https://doi.org/10.1016/j.sna.2022.113552

Żołek-Tryznowska, Z., & Cichy, Ł. (2018). Glycerol derivatives as a modern plasticizers for starch films. In 9th *International symposium on graphic engineering and design* (pp. 217-221). The University of Novi Sad. https://doi.org/10.24867/GRID-2018-p27